Journal of Materials Chemistry A

PAPER

View Article Online
View Journal | View Issue

Cite this: J. Mater. Chem. A, 2015, 3, 2097

Magnetic and conductive graphene papers toward thin layers of effective electromagnetic shielding†

Wei-Li Song,[a] Xiao-Tian Guan,[a] Li-Zhen Fan,*[a] Wen-Qiang Cao,[b] Chan-Yuan Wang,[d] Quan-Liang Zhao[c] and Mao-Sheng Cao*[b]

Received 4th November 2014
Accepted 21st November 2014

DOI: 10.1039/c4ta05939e

www.rsc.org/MaterialsA

Graphene-based hybrids, specifically free-standing graphene-based hybrid papers, have recently attracted increasing attention in many communities for their great potential applications. As the most commonly used precursors for the preparation of graphene-based hybrids, electrically-insulating graphene oxides (GO) generally must be further chemically reduced or thermally annealed back to reduced GO (RGO) if high electrical conductivity is needed. However, various concerns are generated if the hybrid structures are sensitive to the treatments used to produce RGO. In this work, we develop a highly facile strategy to fabricate free-standing magnetic and conductive graphene-based hybrid papers. Electrically conductive graphene nanosheets (GNs) are used directly to grow Fe_3O_4 magnetic nanoparticles without additional chemical reduction or thermal annealing, thus completely avoiding the concerns in the utilisation of GO. The free-standing Fe_3O_4/GN papers are magnetic, electrically conductive and present sufficient magnetic shielding (>20 dB), making them promising for applications in the conductive magnetically-controlled switches. The shielding results suggest that the Fe_3O_4/GN papers of very small thickness (<0.3 mm) and light weight (~0.78 g cm^{-3}) exhibit comparable shielding effectiveness to polymeric graphene-based composites of much larger thickness. Fundamental mechanisms for shielding performance and associated opportunities are discussed.

1. Introduction

Since great advancements have been made in the electronic and communication industries, unexpected electromagnetic irradiation generated by mobile phones, digital devices, and communicating devices is currently a significant concern in society.[1–4] Due to their effective blocking and attenuation of electromagnetic waves, electromagnetic shielding materials have attracted increasing interest for suppressing and diminishing the impact of the irradiation.[5–10] Carbon-based materials and composites have been widely developed for their unique features including excellent corrosion resistance, light weight, and easy processing, which are more advantageous than traditional metals. Among recent efforts, graphene-based composites have received extraordinary attention because of their exclusive characteristics. Specifically, its intrinsic metal-like electrical conductivity arising from its all-carbon two-dimensional configuration and delocalised π electronic network may allow graphene to be ideally suited for electromagnetic shielding.[11,12]

Attempts have focused on the fabrication of polymeric graphene-based composites with different morphologies and structures.[3,12–16] In a recent study by Chen *et al.*, chemical vapour deposition was used to deposit graphene on Ni-foam frameworks, and the fabricated graphene/poly(dimethyl siloxane) composite foams with 2 S cm^{-1} possessed a shielding performance of 22–25 dB at a foam thickness of ~1 mm.[3] Moreover, magnetic particles such as well-known magnetite (Fe_3O_4) have also been employed in polymer matrices to prepare polymeric magnetic metal oxides/graphene-based hybrids with the aim of enhancing magnetic attenuation.[17,18] Currently, when large amounts of hydrophilic functional groups and defects are present in graphene oxide (GO), the strategies used to produce magnetic metal oxides/RGO-based hybrids are usually based on the introduction of magnetic metal oxides or related precursors along with the conversion of electrically insulating GO back to electrically conductive reduced GO (RGO).[18–23] For example, in the work by Chung and co-workers, hydrazine was applied in the fabrication of Fe_3O_4/RGO/polyaniline composites, and the results suggest that the composites with electrical conductivity

[a]Institute of Advanced Materials and Technology, University of Science and Technology Beijing, Beijing, 100083, P. R. China. E-mail: fanlizhen@ustb.edu.cn; Tel: +86 10 6233 3548

[b]School of Materials Science and Engineering, Beijing Institute of Technology, Beijing, 100081, P. R. China. E-mail: caomaosheng@bit.edu.cn; Tel: +86 10 6891 4062

[c]School of Electrical and Mechanical Engineering, North China University of Technology, Beijing, 100144, P. R. China

[d]310 Department, Third Institution of China Aerospace Science & Industry, Beijing 100071, P. R. China

† Electronic supplementary information (ESI) available: SEM images of the cross-sectional views of more Fe_3O_4/GN papers, the relationship between saturation magnetisation and Fe_3O_4 loading and images of the fabrication of Fe_3O_4/GO hybrids with 50 wt% Fe_3O_4. See DOI: 10.1039/c4ta05939e

up to 2.6 S cm^{-1} exhibited absorption shielding of ~26 dB when the composite thickness was 2.5 mm.[19] Zheng and co-workers used a similar procedure to prepare polymeric RGO/Fe_3O_4 composite foams that exhibited a shielding performance of up to 19 dB at a thickness of 2.5 mm.[18]

On the other hand, shielding materials with small thicknesses are also demanded in slim devices and other fields where thin layers and interfaces for blocking electromagnetic waves are required.[24–27] According to a previous report,[18–23] employing polymers in Fe_3O_4/RGO-based hybrids may not be suitable since the introduction of polymers with poor electrical conductivities would greatly decrease the electrical conductivity, resulting in enlarged thickness and volume in the composites.[26,27] Instead, the utilisation of all-carbon or polymer-free structures with greatly enhanced electrical properties can substantially reduce the material thickness by decreasing the skin depth.[11,15,28] Very recently, Song *et al.* developed all-carbon shielding materials that show effective shielding performance (>20 dB commercial level) at a very small thickness (less than 0.3 mm).[26,27] This indicates that the exploration of polymer-free Fe_3O_4/graphene hybrids could be a promising strategy for meeting this requirement.

Although plenty of works have reported approaches for preparing polymer-free metal oxide/RGO hybrids, which are known as free-standing or self-supporting RGO-based papers in some free-standing thin products,[29–31] the use of RGO for fabricating electrically conductive RGO-based papers still faces undesirable shortcomings. In the conversion of GO back to RGO, the reducing agents and temperature for thermal annealing essentially depend on the chemical structures and components of both the metal oxides and GO,[32–34] and unexpected weight losses, morphological and phase changes, and other related concerns arise during the treatments. As a consequence, the recovery of electrical conductivity in RGO is generally insufficient if the introduced metal oxides are sensitive to the treatments. In the present work, we demonstrate a simple approach for fabricating novel magnetic and conductive free-standing Fe_3O_4/graphene papers using highly conductive graphene nanosheets (GNs) as the matrix for the direct growth of Fe_3O_4. In this approach, the concerns involved in the recovery of electrical conductivity from GO are entirely avoided. The resulting Fe_3O_4/GN papers present high electrical and magnetic properties and thus could be directly used as conductive magnetic-controlled switches and ultrathin layers for electromagnetic shielding. These papers have a thickness of less than 0.3 mm, a shielding performance of up to 24 dB (>20 dB, the level for commercial application), and a similar density (~0.78 g cm^{-3}) to some polymeric foams, suggesting more promising potential compared to other polymeric graphene-based composites of much larger thickness. The opportunities of such thin shielding papers along with the related shielding mechanism have been further discussed.

2. Results and discussion

As illustrated in Fig. 1, magnetic and conductive Fe_3O_4/GN papers were simply prepared by hydrothermal treatment with

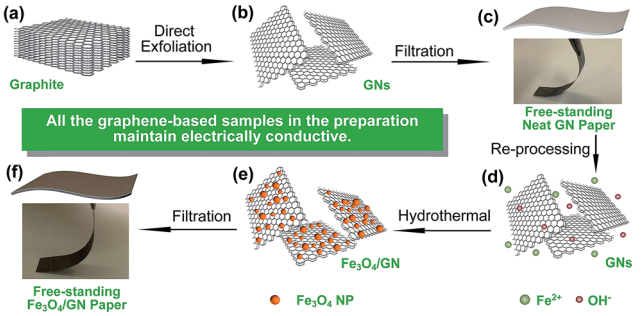

Fig. 1 Schemes of the fabrication of free-standing magnetic and conductive Fe_3O_4/GN papers *via* conductive neat GN papers. Note that all the samples used in this process were conductive; thus, no additional chemical reduction or thermal annealing was required.

hydrophilic and conductive GNs. Briefly, GNs that were directly exfoliated from expanded graphite, as reported in our previous work (Fig. 1a and b),[26,27] could be easily fabricated into free-standing conductive GN papers (>20 000 S m^{-1}) without any further chemical reduction or thermal annealing (Fig. 1c). Since a slight amount of hydroxyl and carboxyl groups were introduced on the surface (O% < 9%),[26] the GN papers were able to be re-processed to form a uniform GN aqueous suspension, enabling GNs to be decorated with magnetic Fe_3O_4 nanoparticles (NPs) in a mixed aqueous solution of $FeSO_4 \cdot 7H_2O$ and NaOH (Fig. 1d). Upon a simple one-step hydrothermal treatment, the as-prepared Fe_3O_4/GN hybrids could be filtrated to form magnetic and conductive Fe_3O_4/GN papers (Fig. 1e and f). Similar to the neat GN papers, the dried Fe_3O_4/GN papers could be peeled off from the filter-membranes, and they were also free-standing and bendable (Fig. 1f). Fe_3O_4/GN papers containing different amounts of Fe_3O_4 NPs were obtained by changing the concentrations of $FeSO_4 \cdot 7H_2O$ in the mixed solution for hydrothermal treatments (Table 1).

Unlike in recent reports on conductive RGO-based hybrid structures in which the employed procedures mostly involved the utilisation of GO and the further recovery of conductivity,[18–23,35–38] the sp^2 hybridisation (referring to conductive characteristic) of the GNs used herein is well preserved;[26] thus, conduction recovery and related concerns could be completely avoided. Therefore, the subsequent introduction of a hetero-compound on the GN surface could be easily achieved due to the presence of hydrophilic functional groups. Meanwhile, high

Table 1 Magnetic properties of the samples (M_s: saturation magnetisation; H_c: coercivity; M_r: remnant magnetisation)

Samples	Fe_3O_4 loading (wt%)	M_s (emu g^{-1})	H_c (G)	M_r (emu g^{-1})
Neat Fe_3O_4 NPs	100	106	79	12
Neat GN paper	0	<0.1	2661	<0.1
Fe_3O_4/GN-1 paper	16	11	92	1
Fe_3O_4/GN-2 paper	28	23	93	3
Fe_3O_4/GN-3 paper	37	31	96	4
Fe_3O_4/GN-4 paper	50	47	91	6

conductivities could be achieved in the resulting GN-based hybrid structures.

2.1 Material characterisation

Fig. 2 shows the typical field-emission scanning electron microscopy (SEM) images of the samples. As shown in Fig. 2a, the neat Fe_3O_4 NPs clusters prepared in the absence of GN are of the order of 100–200 nm, similar to the cluster size observed in the Fe_3O_4/GN hybrids (Fig. 2b). The cross-sectional views of the free-standing neat GN papers and Fe_3O_4/GN papers with the highest particle loadings (50 wt%) are shown in Fig. 2c and e, respectively. Along with more cross-sectional SEM images of other samples with different particle loadings (Fig. S1†), these images suggest that the well-aligned GNs and their intimate stacking (Fig. 2c) in the neat GN papers was greatly impacted by the introduction of particles on the GN surface, leading to degraded anisotropic characteristics in the Fe_3O_4/GN papers (Fig. 2e and f, S1e and S1f†). The top views imply that the neat GN papers (Fig. 2d) and the Fe_3O_4/GN papers (Fig. 2g) are not significantly different, with the exception of the presence of particle clusters in the Fe_3O_4/GN papers (Fig. 2g and h).

Representative transmission electron microscopy (TEM) images of the as-prepared Fe_3O_4/GN hybrids are shown in Fig. 3. According to Fig. 3a and b, the diameter of single nanoparticles in the clusters is around 30–60 nm. X-ray powder diffraction (XRD) spectra (Fig. 4a) show that the estimated average thickness of the GN used in this work is less than 8 nm (according to the Scherrer equation), which is consistent with the results of our previous work.[26] Apart from the GN peaks, the other peaks in the XRD spectrum of the Fe_3O_4/GN papers are assigned to mixed-valence inverse-spinel iron oxide Fe_3O_4 (JCPDS card no. 88-0315). Additionally, the high-resolution TEM (HRTEM) image (Fig. 3c) and selected-area electron diffraction (SAED) patterns (Fig. 3d) of the particles in the Fe_3O_4/GN hybrids suggest that the lattice spacing is around 0.29 nm, corresponding to the *d*-spacing of the (220) crystal plane of Fe_3O_4.

X-ray photoelectron spectroscopy (XPS) was performed to determine the surface components of the Fe_3O_4/GN papers (Fig. 4b). In the neat GN papers, the elemental concentrations of C and O were 90.36% and 8.71%, respectively, with ignorable N element content (<1%) introduced in the exfoliation process.[26] In our previous work, the detected O content (8.71%) in the neat GN papers was assigned to be the contribution of C–O and C=O species associated with hydroxyl and carboxyl functional groups, which could provide nucleation points (*via* attracting cations) for the formation of hetero-compounds (metal oxides in this case). As shown in Fig. 4c, the C1s spectrum of the Fe_3O_4/GN papers also indicates the presence of C–O and C=O species located at 286.1 and 287.8 eV, respectively. Moreover, the Fe2p spectrum (Fig. 4d) suggests that the two pronounced peaks detected at 711.0 and 724.2 eV correspond to $Fe2p_{3/2}$ and $Fe2p_{1/2}$, respectively.[39] Accordingly, the fitting results imply that the concentrations of Fe(II) and Fe(III) are estimated to be 33.76% and 66.24%, respectively, almost corresponding to their molar ratio (1 : 2) in Fe_3O_4. The XPS results of Fe_3O_4 are in good agreement with the above XRD and HRTEM analyses.

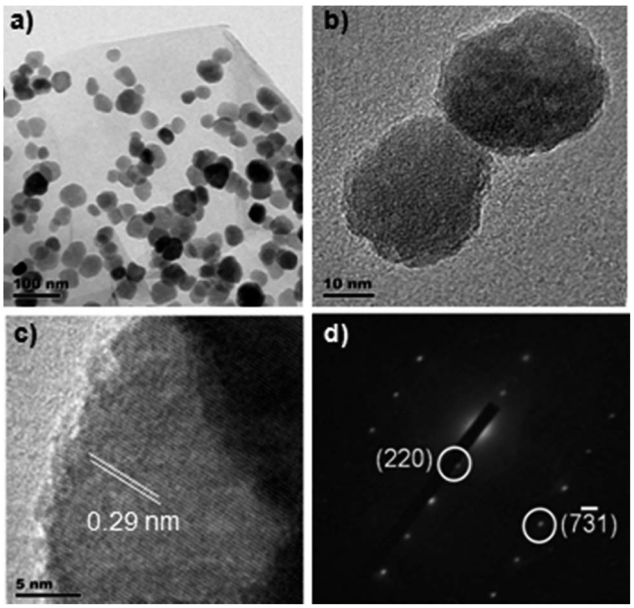

Fig. 3 Typical TEM images of Fe_3O_4/GN (a) and Fe_3O_4 NPs on the GN (b) and (c); SAED patterns of the Fe_3O_4 NPs (d).

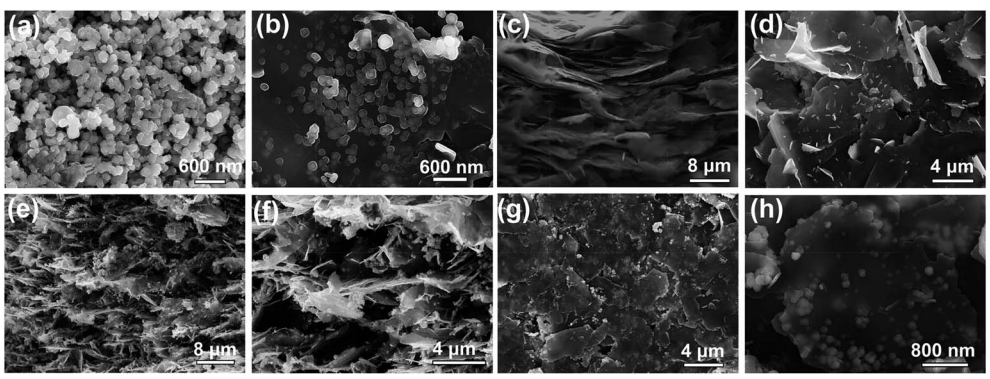

Fig. 2 Typical SEM images: neat Fe_3O_4 NPs (a) and Fe_3O_4/GN (b); cross-sectional view (c) and top view (d) of the neat GN paper; cross-sectional view (e) and (f) and top view (g) and (h) of the Fe_3O_4/GN-4 paper.

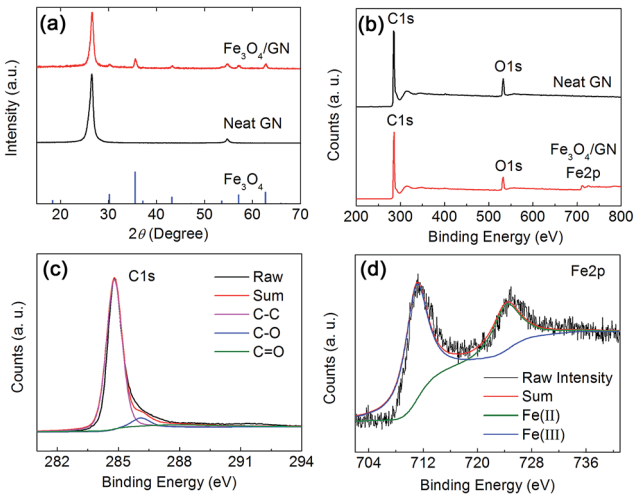

Fig. 4 XRD spectra (a) and XPS spectra (b) of the samples as marked; C1s (c) and Fe2p (d) spectra of the Fe_3O_4/GN papers.

According to the morphological and structural characterisations, the size of the introduced Fe_3O_4 NPs and their clusters are almost 10 or even 100-fold larger than the thickness of a single piece of GN, which greatly affects the interface and interaction of the Fe_3O_4/GN hybrids (Fig. 5a and b). Aside from the considerable changes observed in the GN stacking (Fig. 2), it is interesting that the Fe_3O_4/GN hybrids were also able to form free-standing GN papers in the presence of Fe_3O_4 NPs (Fig. 2 and 3); this was even achieved by the Fe_3O_4/GN hybrids with Fe_3O_4 loadings up to 50 wt%. As discussed previously, the formation mechanism of the neat GN papers strongly depends on the compression of the air–water interface and, more importantly, the hydrogen bonding *via* the hydroxyl and carboxyl groups on the GN surface (Fig. 5c).[40] In the case of Fe_3O_4/GN hybrids, un-nucleated polar sites including hydroxyl and carboxyl groups on the GN surface may attach to iron oxide NPs.[41] In particular, hydrogen bonding would be generated between GNs and the Fe_3O_4 NPs formed in the aqueous solution with a high concentration of OH^- groups (Fig. 5d).[41] Owing to the physical and chemical interactions, the resulting Fe_3O_4/GN hybrids can form free-standing magnetic and conductive papers for potential applications in many fields.

2.2 Electrical and magnetic properties

The as-fabricated free-standing Fe_3O_4/GN papers with a thickness around ~100 microns were directly settled on a classic four-probe setup to measure the electrical properties. As shown in Fig. 6a, the estimated electrical conductivities (EC) of the GN papers with different Fe_3O_4 loadings are plotted based on

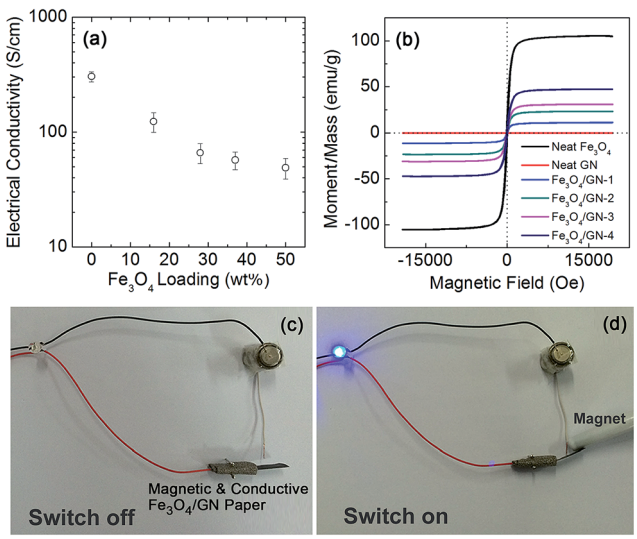

Fig. 6 Electrical conductivities (a) and magnetic properties (b) of the GN papers with different Fe_3O_4 loadings; a demonstration of the Fe_3O_4/GN-4 paper used as a magnetically-controlled switch in a circuit (c) and (d).

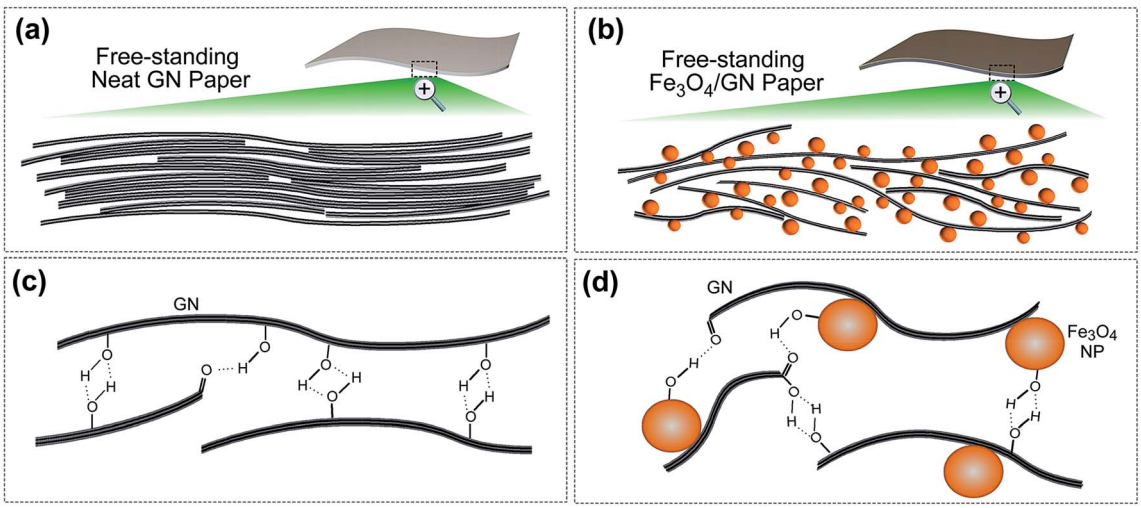

Fig. 5 Schemes of the cross-sectional illustrations of the free-standing GN paper (a) and Fe_3O_4/GN paper (b); possible mechanism of the interactions between GN layers in the neat GN paper (c) and interactions between Fe_3O_4/GN sheets (d).

calculations from the recorded surface resistances and paper thicknesses. The average EC was found to decrease with increasing Fe_3O_4 loading, with sample EC values of ~300, ~120, ~66, ~57 and ~50 S cm^{-1} (Fig. 6a). This decrease is attributed to the fact that the introduction of electrically insulating Fe_3O_4 at the GN interfaces could lead increased interfacial resistance. For a direct comparison, the Fe_3O_4/GN papers with 16 wt% and 50 wt% Fe_3O_4 in this work possess EC values of ~120 and ~50 S cm^{-1}, respectively, which are still higher than the EC values of the previously reported Fe_3O_4/RGO papers (EC < 40 S cm^{-1}) with less than 8 wt% Fe_3O_4.[22] The possible reason for the lower EC is that reservation of Fe_3O_4 in those GO papers might limit the utilisation of very harsh reduction or high-temperature annealing for recovering EC in RGO; thus, the reduction of GO by thermal annealing at only 400 °C was relatively insufficient.[22] As a consequence, use of GN papers as the matrix in this study seems to be more promising for the fabrication of highly electrically conductive graphene-based hybrids.

In the investigation of magnetic properties, a magnetic field ranging from −20 000 to 20 000 Oe was applied at room temperature; the magnetisations of the samples are shown in Fig. 6b. According to the curves in Fig. 6b, the saturation magnetisations, coercivities and remnant magnetisations of the samples are listed in Table 1. With increasing Fe_3O_4 loading, the saturation magnetisation increased linearly in the Fe_3O_4/GN samples (Fig. S2†). The highest saturation magnetisation of the Fe_3O_4/GN sample (50 wt% Fe_3O_4) approaches 47 emu g^{-1}, almost 45% of the intensity found in the neat Fe_3O_4 sample. Similarly, the change in remnant magnetisation in the Fe_3O_4/GN samples was also nearly linear Fe_3O_4 content (Table 1). The introduction of Fe_3O_4 dramatically suppressed the coercivities of the hybrid samples compared to that of the neat GN.

To take advantage of the free-standing magnetic and conductive papers, a piece of the Fe_3O_4/GN papers with an Fe_3O_4 loading of 50 wt% was stabilised in a homemade circuit switch (Fig. 6c). When a magnet was used to remotely attract the magnetic Fe_3O_4/GN paper, it was instantaneously driven toward the magnet, and the light in the circuit was turned on, as expected (Fig. 6d). In comparison with traditional mechanical switch- and relay-based iron films, the magnetic and conductive Fe_3O_4/GN papers with unique features including easy processing, corrosion resistance and light weight produced in this work may serve as novel magnetic-controllable switches in various circuits and related electric fields.

2.3 Electromagnetic shielding performance and mechanism

To investigate the electromagnetic shielding of the magnetic and conductive Fe_3O_4/GN papers, they were fabricated into two dielectric sheets to form a sandwich structure.[15,26,27] In general, the primary mechanism of EMI attenuation and shielding involves the combination of reflection, absorption attenuation and multiple reflections. Reflection attenuation (SE_{ref}) relies on the impedance mismatch at the interface between air and the shielding materials, and the dielectric sheets in our sandwich structure were considered as a medium close to air.[42–45] Absorption attenuation (SE_{abs}) is associated with the electromagnetic energy conversion, and the electromagnetic energy could be consumed by conversion into leaking current or heat in the shielding materials.[42–45] Multiple reflections could be ignored in our case because the thickness of the Fe_3O_4/GN papers used for shielding measurement was in the range of 200–250 microns, which is larger than the estimated skin depth.[11,15,28]

Unlike ideal conductors, where an electric field cannot exist inside the highly electrically conductive metal material, and electromagnetic waves will thus be mostly reflected, the Fe_3O_4/GN papers in this study are penetrated by the electromagnetic waves (Fig. 7). As a result (Fig. 7c), the reflected electromagnetic waves at the interface and penetrating waves could follow Snell's law.[45,46] When the incident waves are perpendicular to the interface (Fig. 7), Snell's law can be simplified as

$$r = \frac{n_0 - n_1}{n_0 + n_1} \quad (1)$$

$$p = \frac{2n_0}{n_0 + n_1} \quad (2)$$

$$n = \sqrt{\varepsilon_r \mu_r} \quad (3)$$

where r and p are reflection and penetration, respectively, and n_0 and n_1 are the indices of refraction of air and the samples, respectively. For the refractive index of electromagnetic radiation in eqn (3), ε_r and μ_r are the medium's relative permittivity and relative permeability, respectively.[45–47] According to eqn (1) and (2), an increased index of refraction in the shielding samples would lead to larger reflection and reduced penetration. Additionally, the relative permittivity of lossy materials and the actual electrical conductivity can be formulated as:

$$\varepsilon_r = \varepsilon_r' + \frac{i\sigma}{\omega\varepsilon_0} \quad (4)$$

where ε_r' is the real permittivity, σ the electrical conductivity, ω is the angular frequency and ε_0 is the electric constant. In typical shielding materials of dielectric loss such as non-magnetic carbon-based composites (where $n^2 = \varepsilon_r$), it is clear that the SE_{ref} of the composites was enhanced monotonically with increasing carbon filler loading.[15] This phenomenon is caused by the monotonic enlargement of refractive index due to the increase in electrical conductivity according to eqn (1), (3) and (4). For the case of the magnetic and conductive Fe_3O_4/GN papers in this work, however, the refractive index is determined by both relative permittivity and relative permeability. With the increase of Fe_3O_4 in the Fe_3O_4/GN papers, electrical conductivity was monotonically decreased (Fig. 6a), while the magnetic properties exhibited the opposite trend (Table 1; assuming that the magnetic properties in the Fe_3O_4 NPs maintain the same level, and the magnetic properties of the Fe_3O_4/GN papers are thus mainly proportional to the Fe_3O_4 loadings). Therefore, as a result of the competition between electrical and magnetic properties, the samples with 37 wt% Fe_3O_4 (Fe_3O_4/GN-3) present the optimal SE_{ref} among the four Fe_3O_4/GN papers (Fig. 8a and b).

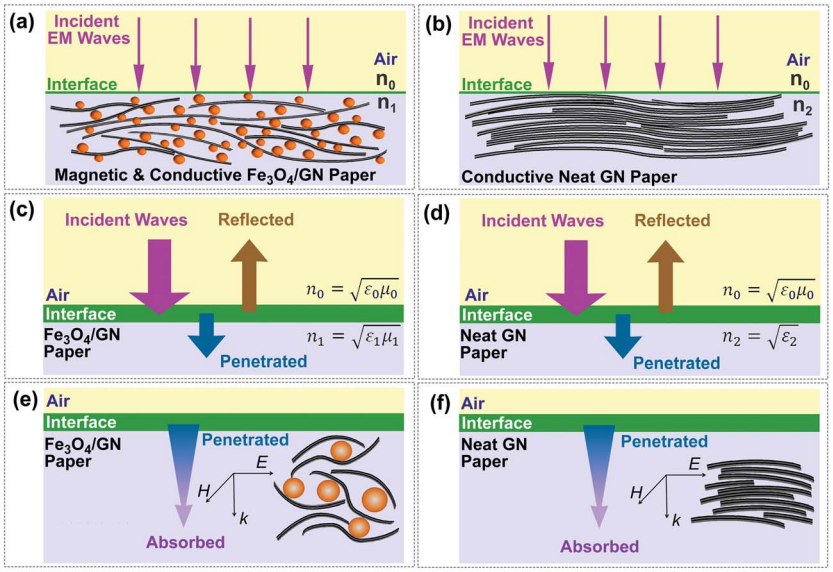

Fig. 7 Schemes of the propagation of electromagnetic waves when they meet the neat GN (a) and Fe_3O_4/GN papers (b); reflection at the surface (c) and absorption in the Fe_3O_4/GN paper (e); reflection at surface (d) and absorption in neat GN paper (f).

Penetrating into the Fe_3O_4/GN papers, the electromagnetic waves were gradually consumed by the Fe_3O_4/GN papers in terms of absorption and other conversions, which could be generally described as:[11,15]

$$SE_{abs} = 8.686d\sqrt{\pi f \sigma \mu}\ \text{dB} \quad (5)$$

where d is the thickness of the Fe_3O_4/GN papers (200–250 micron), f is the frequency, and $\mu = \mu_0\mu_r$, where μ_0 is a constant. Upon absorption attenuation in the Fe_3O_4/GN papers, electromagnetic waves could be simultaneously consumed by both electrical and magnetic loss, which is attributed to the generation of leaking current in the graphene-based conductive networks[11,15,48] and loss caused by magnetic dipoles in the Fe_3O_4 particles,[5,10,49–51] respectively. According to eqn (5), the electrical and magnetic properties also play competitive roles in the SE_{abs} with a different functional form. Consequently, the results show that SE_{abs} presents monotonic improvement with increasing Fe_3O_4 loading (Fig. 8c and d), indicating that the magnetic loss may dominantly contribute to electromagnetic attenuation at higher Fe_3O_4 loadings. Accordingly, the highest SE_{abs} (13–17 dB) appears in the samples with 50 wt% Fe_3O_4 (Fe_3O_4/GN-4), as shown in Fig. 8c. Additionally, according to eqn (5), it should be emphasised that SE_{abs} is also significantly dependent on the thickness of the shielding materials; thus, SE_{abs} could be easily altered based on the material thickness.[11,15,26] This is completely

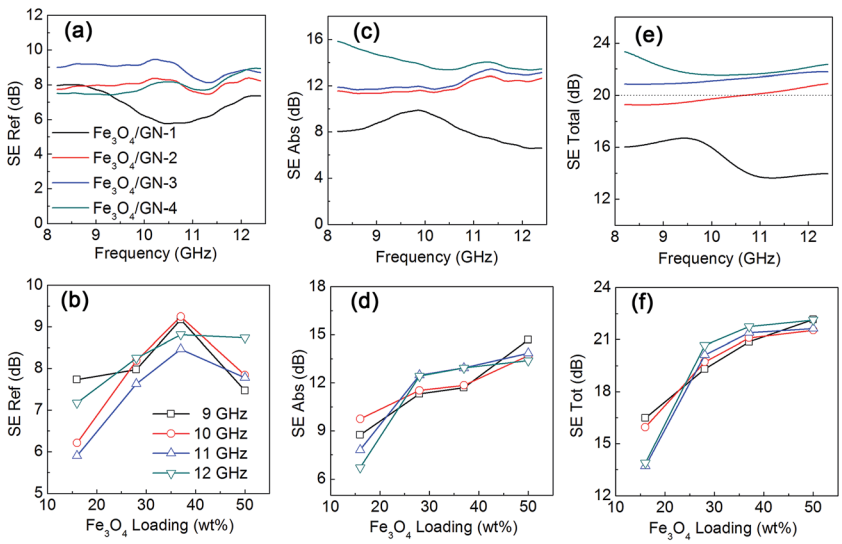

Fig. 8 Shielding performance of the Fe_3O_4/GN papers: SE_{ref} (a), SE_{abs} (c) and total shielding effectiveness (e) with change of frequency; SE_{ref} (b), SE_{abs} (d) and total shielding effectiveness (f) with change in Fe_3O_4/GN loading.

distinct from SE_{ref}, which primarily relies on the interfacial conditions between transport media and is insensitive to material thickness.[15,21,26]

The total SE performances of the Fe_3O_4/GN papers are demonstrated in Fig. 8e and f, showing that total SE increases monotonically with increasing Fe_3O_4 loading. The optimal shielding performance reaches 21–24 dB, which meets the requirement for commercial applications. Table 2 lists recently reported graphene-based shielding materials. As mentioned previously, SE_{abs} is proportional to material thickness; therefore, it is a great challenge to achieve effective shielding performance at very small thicknesses. According to Table 2, the Fe_3O_4/GN papers with thicknesses smaller than 0.25 mm in this work present highly competitive shielding performances compared to other polymeric graphene-based composites with thicknesses larger than 1 mm. For example, Shen *et al.* fabricated polymeric RGO/Fe_3O_4 composite foams that exhibited an optimised shielding performance of 15–19 dB at a thickness of 2.5 mm.[18] In another recent work by Singh *et al.*, RGO/Fe_3O_4/polyaniline composites with thicknesses of 2.5 mm showed absorption shieldings up to 26 dB, approaching total shielding performance around 29–31 dB.[19] On the basis of the previous reports in Table 2, it is apparent that the employment of polymers with much lower electrical conductivities than graphene (or RGO) essentially enlarge interfacial and contact resistance. In addition, the presence of Fe_3O_4 may simultaneously limit the recovery of electrical conductivity in RGO, as discussed above. Consequently, much larger thicknesses must be made to reach the target shielding performance in these polymeric RGO/Fe_3O_4 composites. On the contrary, polymers (or additives) of poorer conductance have been completely avoided in the design of Fe_3O_4/GN papers in this study, allowing high electrical conductivity to be achieved. In contrast to the inferior electrical conductivities of the other shielding composites (Table 2), the high electrical and magnetic properties of the self-supported Fe_3O_4/GN papers allow them to present sufficient shielding performances at much smaller thicknesses. Additionally, it is interesting to observe that the Fe_3O_4/GN paper with 50 wt% Fe_3O_4 possesses a decreased density of around ~0.78 g cm^{-3}, much smaller than the denser neat GN paper (~1.6 g cm^{-3}) due to the change in GN stacking by the introduction of Fe_3O_4 on the GN surface. As a result, the porous GN-based nanostructures allowed the Fe_3O_4/GN papers to present very similar densities to some polymeric foam composites (*e.g.*, ~0.79 g cm^{-3} for RGO/PMMA foams).[52] Hence, the thin Fe_3O_4/GN papers with high electrical conductivities in this study are promising for applications in lightweight electromagnetic shielding coatings and other fields, especially when an ultrathin layer or interface is required.

2.4 More discussion

Although the neat GN papers possess comparable shielding performance to the Fe_3O_4/GN-4 papers (Fig. 9), the mechanisms of SE_{abs} and SE_{ref} in these two samples are dissimilar (Fig. 7). For the SE_{ref} at the interface, relative permittivity is the only parameter affecting the reflection in non-magnetic neat GN papers (where $n^2 = \varepsilon_r$; Fig. 7d). Even though the electrical conductivity of neat GN paper (~300 S cm^{-1}) is several-fold higher than that of Fe_3O_4/GN-4 paper (~50 S cm^{-1}), Fig. 9b indicates that the contribution of magnetic properties substantially improved the SE_{ref} of Fe_3O_4/GN-4. On the other hand, magnetic loss is one of the different mechanisms in the absorption shielding between the neat GN and Fe_3O_4/GN-4 papers. Additionally, the change in GN stacking (Fig. S1†) caused by the Fe_3O_4 NPs led to decreased anisotropy in the Fe_3O_4/GN-4 papers. In our previous work, GN stacking with highly anisotropic character significantly improved both SE_{abs} and SE_{ref}.[55] For the neat GN paper (Fig. 7f), the electric field (E) of electromagnetic waves perpendicular to the traveling direction (k) is parallel to the planar direction of GN stacking, where the electrical loss induced by leaking current will be maximised.[55] However, this loss will be largely reduced in the Fe_3O_4/GN-4 papers (Fig. 7e) due to the less anisotropic character in the GN stacking. Therefore, the comparison of the two samples suggests that the introduction of Fe_3O_4 NPs in the GN papers affects the shielding mechanisms in terms of changes in surface reflection, leaking current, magnetic loss and attenuation induced by anisotropic character. Based on the combination of the samples in this work, a rough scheme was illustrated to demonstrate the relationships between shielding performance and electrical/magnetic properties (Fig. 10).

Table 2 Comparison of typical graphene-based shielding materials (PMMA: polymethyl methacrylate; PS: poly styrene; PEI: poly etherimide; PDMS: poly dimethylsiloxane; TMAH: tetramethylammonium hydroxide; PANI: poly-aniline)

Fillers	Matrices/additives	Thickness (mm)	Electrical conductivity (S cm^{-1})	Shielding performance (dB)	Ref.
CVD-growth graphene	PDMS	1.0	2	22–25	3
Functionalised graphene	PS	2.5	0.01	25–29	13
RGO	PEI	2.3	0.00001	18–22	53
RGO	PMMA	2.4	0.03	13–19	52
RGO	SiO_2	1.5	0.12	34	4
MWCNT/graphite	PS	5.6	0.0095	20	54
Fe_3O_4/RGO	PEI	2.5	—	14–18	18
Fe_3O_4/RGO	TMAH (surfactant)	3	0.1	41	9
Fe_3O_4/RGO	PANI	3.34	2.6	29–31	19
Fe_3O_4/GN	—	0.20–0.25	50	21–24	In this work

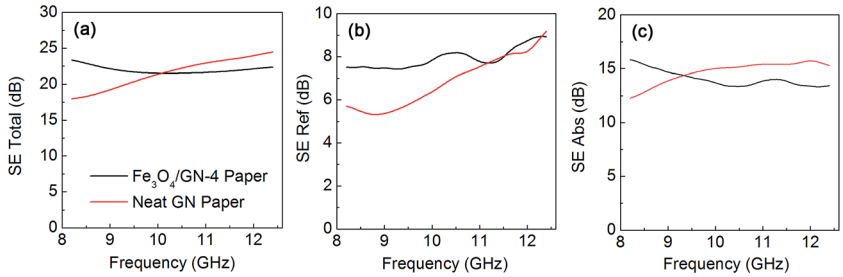

Fig. 9 Comparison of shielding performance between the neat GN paper and Fe_3O_4/GN-4 paper: total shielding effectiveness (a), SE_{ref} (b) and SE_{abs} (c) with change in frequency.

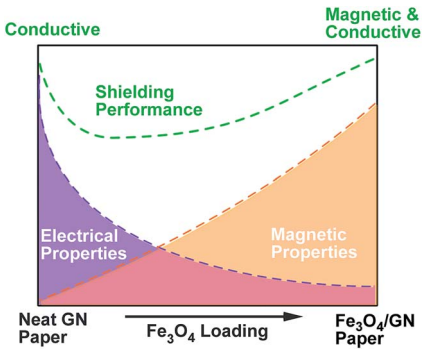

Fig. 10 Scheme of the shielding performance in the thin-layer GN-based papers: relationship with the changes in both electrical and magnetic properties.

Furthermore, we attempted to fabricate free-standing Fe_3O_4/RGO hybrid papers of 50 wt% Fe_3O_4 under the same conditions using the same amount of GO instead of GN. Unfortunately, free-standing papers were not achieved, and cracks were observed in the Fe_3O_4/RGO hybrids (Fig. S3†). In a recent report, Liu and co-workers found that it is difficult to prepare free-standing RGO-based hybrid papers when introducing high-loadings of metal oxides; however, in that study, additional carbon nanotubes were simultaneously used.[56] Therefore, it is suggested that facile methods for fabricating Fe_3O_4/GN are much more advantageous, particularly in the fabrication of free-standing graphene-based hybrid papers with high-loadings of metal oxides.

As discussed above, the utilisation of GN in the preparation of magnetic and conductive Fe_3O_4/GN papers is relatively simple, and the concerns related to the post-treatment of GNs are totally averted. This strategy could be extensively applied in a wide variety of fields where the introduced hetero-compounds are sensitive to the treatments for RGO-based hybrids, specifically in cases where graphene-based hybrids with high electrical conductivities are needed. Furthermore, the advantages of such Fe_3O_4/GN papers including light weight, bendability, ease of processing, electrical conductivity and magnetic features enable them to be used in electronic technologies and industries such as magnetically-controlled systems and electromagnetic shielding coatings.

3. Conclusions

In summary, the simple fabrication of novel free-standing magnetic and conductive Fe_3O_4/GN papers has been demonstrated. This strategy shows more advantages than the utilisation of GO for achieving conductive graphene-based hybrid structures. The good magnetic and electrical properties allow them to be applied in the conductive magnetically-controlled switches and thin layers for electromagnetic shielding. Their shielding performance suggests that the thin Fe_3O_4/GN papers are highly competitive with other graphene-based composites of much larger thicknesses. Therefore, the results indicate that the proposed simple strategy can be widely applied in many fields for preparing conductive lightweight graphene-based hybrids, specifically for materials that are sensitive to harsh chemical or thermal treatments. Moreover, the free-standing magnetic and conductive papers have several advantages, giving them potential applications beyond those of graphene-based bulk hybrids.

4. Experimental section

4.1 Neat GN papers

Neat GN papers were prepared according to our previous work.[26] In brief, a commercial graphite sample (0.5 g, grade 3805 from Asbury Carbons) was pre-treated in an aqueous solution of alcohol under stirring and sonication. The dried pre-treated samples were further dispersed in a mixed solution of nitric acid and sulphuric acid under sonication (48–72 h) for direct chemical exfoliation. The resulting samples were transferred to 2 l of water and diluted with abundant water. After the diluted aqueous suspension was sonicated for 1 h, the suspension was filtered to obtain GN papers. The as-fabricated neat GN paper was dried in a vacuum oven and then peeled off for the preparation of Fe_3O_4/GN papers.

4.2 Fe_3O_4/GN papers

A portion of the as-prepared neat GN paper (50 mg) was transferred to 10 ml of water. A vigorous needle-sonication was utilised to re-disperse the GN paper in the water until no precipitate was observed. The as-treated suspension was then sonicated for another 2 h. Subsequently, $FeSO_4 \cdot 7H_2O$ (70 mg) was added to 4 ml of water and stirred until $FeSO_4 \cdot 7H_2O$ was

dissolved. The solution was added dropwise into the above GN aqueous suspension followed by stirring for 30 min and the addition of NaOH solution (20 mg NaOH in 4 ml H_2O). The mixture was then transferred to a Teflon-lined stainless steel autoclave for hydrothermal reaction at 180 °C for 10 h. After natural cooling to room temperature, the sample filtered and washed several times with water. The clean sample was dried in a vacuum oven at 80 °C and then peeled off to obtain free-standing Fe_3O_4/GN paper. To produce papers with different thicknesses, the amounts of hydrothermally-treated Fe_3O_4/GN suspension used for filtration were scaled up based on the required thickness.

For the reference samples, neat Fe_3O_4 particles were prepared using the sample hydrothermal procedure without the GN suspension. For the Fe_3O_4/GN papers with different Fe_3O_4 NP loadings, the amounts of $FeSO_4 \cdot 7H_2O$ used in the hydrothermal treatment were as follows: Fe_3O_4/GN-1, 35 mg $FeSO_4 \cdot 7H_2O$; Fe_3O_4/GN-2, 70 mg $FeSO_4 \cdot 7H_2O$; Fe_3O_4/GN-3, 105 mg $FeSO_4 \cdot 7H_2O$; and Fe_3O_4/GN-4, 175 mg $FeSO_4 \cdot 7H_2O$.

4.3 Graphene oxide (GO)

GO was prepared according to the modified Hummers method.[57] In brief, graphite (2 g) and $NaNO_3$ (1 g) were added to 120 ml of 98% H_2SO_4 in an ice bath. The mixture was kept at 0 °C for 1 h followed by the gradual addition of $KMnO_4$ (6 g). After stirring for 2 h, the mixture was heated and kept at 30 °C for 0.5 h. Subsequently, water (150 ml) was added dropwise followed by the addition of H_2O_2 (5%, 50 ml). Finally, the solution was washed with water and HCl (5%) to obtain the GO aqueous solution.

4.4 Circuit and switch

In the setup of a circuit, a piece of Fe_3O_4/GN-4 paper (30 × 5 mm^2) was settled with a piece of nickel foam and then connected with an LED light and a battery to form a circuit. For the magnetically-controlled switch, a distance (~4 mm) between the end of the Fe_3O_4/GN-4 paper and the conductive wire was included to allow for the movement of the Fe_3O_4/GN-4 paper. A magnet was used as the attractive force to make the Fe_3O_4/GN-4 paper move, and the light in the circuit was "on" or "off" when the Fe_3O_4/GN-4 paper was connected or disconnected to the wire, respectively.

4.5 Layered structures

For the accurate measurement of S parameters, layered structures were fabricated to ensure that the free-standing networks were vertically positioned in the testing chamber.[15,26] Phenolic resin sheets and poly(ethylene-vinyl acetate) (PEVA; DuPont Company) were employed as the dielectric substrates and glue for fabricating the layered structures, respectively. The dielectric substrates were processed into dimensions of 22.86 × 10.16 × 1 mm^3 (size of testing chamber). PEVA was dissolved in toluene followed by the evaporation of most of the solvent to obtain a viscous PEVA/toluene glue. All of the measured free-standing Fe_3O_4/GN papers with thicknesses of 200–250 microns were cut into rectangular shapes of 22.86 × 10.16 mm^2. In the fabrication of dielectric substrates|GN paper|dielectric substrate structures,[15,26] GN paper was sandwiched between two pieces of dielectric substrates with PEVA/toluene glue. Similarly, the dielectric substrates|Fe_3O_4/GN paper|dielectric substrate structure was fabricated using the same approach. All the layered structures were dried in ambient conditions to create the testing samples.

4.6 Characterisations

X-ray photoelectron spectra (XPS) of the GNs were recorded using K-alpha radiation on a Thermo Fisher Scientific ESCALAB 250xi system. Field emission scanning electron microscopy (FE-SEM) images were obtained on a ZEISS supra 55 system. Transmission electron microscopy (TEM) images were obtained on a JEOL JEM-2010 scanning TEM system. The field dependence of magnetisation for the powder samples was measured using a Lake Shore 7410 VSM at room temperature. The as-prepared papers were characterised by various techniques. X-ray diffraction (XRD) characterisation was performed on a PANalytical X'Pert PRO MPD diffraction system. GN thickness was estimated from Scherrer's equation: L_C (rad) = $0.89\lambda/\beta \cos\theta$, where L_C is the average crystallite size (thickness) along the stacking c-axis, λ is the wavelength of the X-ray source (1.5406 Å), β is the full-width-at-half-maximum of the diffraction peak, and θ is the diffraction angle. Electrical conductivity (σ) was determined using the classical four-probe method, and the electrical current (I) and voltage (V) relationship for the networks was obtained by a multimeter (Keithley 2400, controlled by Lab Tracer 2.0 software, both from Keithley Instruments) and a multi-height probe (Jandel). With the relation of network thickness (d), the electrical conductivities of the networks were determined by the equation $\sigma = (\ln 2/\pi)(I/V)/d$. To ensure the accuracy of the electrical conductivity measurements, three different regions of the paper were selected for testing. The average electrical conductivity and corresponding errors of each sample were determined from the three measured values. Density was roughly estimated from the ratio of mass to volume.

4.7 EMI shielding

The S parameters (S_{11} and S_{21}) of the as-fabricated sandwich layered structures were measured on an Anritsu 37269D vector network analyser (VNA) using the wave guide method in the X-band.[15,26] The power coefficients, reflection coefficients (R) and transmission coefficients (T) were calculated by the equations of $R = |S_{11}|^2$ and $T = |S_{21}|^2$, respectively. Electromagnetic shielding effectiveness (SE_{tot}) refers to the logarithm of the ratio of the incident wave P_I to the transmitted wave P_T, which is determined by the equation $SE_{tot} = 10 \log(P_I/P_T)$ dB. The total experimental SE is the sum of the net shielding by reflection (SE_{ref}) and absorption (SE_{abs}), which can be given as $SE_{ref} = -10 \log(1 - R)$ dB and $SE_{abs} = -10 \log(T/(1 - R))$ dB, respectively.[15,26]

Acknowledgements

Financial support from the 973 Project (2013CB934001 and 2015CB932500), the NSF of China (51172024, 51372022, 51302011 and 51305005), the China PSF (2014T70037) and the Fundamental Research Funds for the Central Universities (FRF-TP-14-091A2) is gratefully acknowledged.

References

1 N. Li, Y. Huang, F. Du, X. B. He, X. Lin, H. J. Gao, Y. F. Ma, F. F. Li, Y. S. Chen and P. C. Eklund, *Nano Lett.*, 2006, **6**, 1141–1145.
2 Y. L. Yang, M. C. Gupta, K. L. Dudley and R. W. Lawrence, *Adv. Mater.*, 2005, **17**, 1999–2003.
3 Z. P. Chen, C. Xu, C. Q. Ma, W. C. Ren and H. M. Cheng, *Adv. Mater.*, 2013, **25**, 1296–1300.
4 B. Wen, M. S. Cao, M. M. Lu, W. Q. Cao, H. L. Shi, J. Liu, X. X. Wang, H. B. Jin, X. Y. Fang, W. Z. Wang and J. Yuan, *Adv. Mater.*, 2014, **26**, 3484–3489.
5 D. D. L. Chung, *Carbon*, 2001, **39**, 279–285.
6 F. Moglie, D. Micheli, S. Laurenzi, M. Marchetti and V. M. Primiani, *Carbon*, 2012, **50**, 1972–1980.
7 T. K. Gupta, B. P. Singh, S. R. Dhakate, V. N. Singh and R. B. Mathur, *J. Mater. Chem. A*, 2013, **1**, 9138–9149.
8 D. Micheli, A. Vricella, R. Pastore and M. Marchetti, *Carbon*, 2014, **77**, 756–774.
9 M. Mishra, A. P. Singh, B. P. Singh, V. N. Singh and S. K. Dhawan, *J. Mater. Chem. A*, 2014, **2**, 13159–13168.
10 C. Y. Liang, C. Y. Liu, H. Wang, L. N. Wu, Z. H. Jiang, Y. J. Xu, B. Z. Shen and Z. J. Wang, *J. Mater. Chem. A*, 2014, **2**, 16397–16402.
11 M. H. Al-Saleh and U. Sundararaj, *Carbon*, 2009, **47**, 1738–1746.
12 J. J. Liang, Y. Wang, Y. Huang, Y. F. Ma, Z. F. Liu, J. M. Cai, C. D. Zhang, H. J. Gao and Y. S. Chen, *Carbon*, 2009, **47**, 922–925.
13 D. X. Yan, P. G. Ren, H. Pang, Q. Fu, M. B. Yang and Z. M. Li, *J. Mater. Chem.*, 2012, **22**, 18772–18774.
14 L. Kong, X. W. Yin, X. Y. Yuan, Y. J. Zhang, X. M. Liu, L. F. Cheng and L. T. Zhang, *Carbon*, 2014, **73**, 185–193.
15 W. L. Song, M. S. Cao, M. M. Lu, S. Bi, C. Y. Wang, J. Liu, J. Yuan and L. Z. Fan, *Carbon*, 2014, **66**, 67–76.
16 D. X. Yan, H. Pang, L. Xu, Y. Bao, P. G. Ren, J. Lei and Z. M. Li, *Nanotechnology*, 2014, **25**, 145705.
17 A. P. Singh, P. Garg, F. Alam, K. Singh, R. B. Mathur, R. P. Tandon, A. Chandra and S. K. Dhawan, *Carbon*, 2012, **50**, 3868–3875.
18 B. Shen, W. T. Zhai, M. M. Tao, J. Q. Ling and W. G. Zheng, *ACS Appl. Mater. Interfaces*, 2013, **5**, 11383–11391.
19 K. Singh, A. Ohlan, V. H. Pham, R. Balasubramaniyan, S. Varshney, J. Jang, S. H. Hur, W. M. Choi, M. Kumar, S. K. Dhawan, B. S. Kong and J. S. Chung, *Nanoscale*, 2013, **5**, 2411–2420.
20 Z. S. Wu, Y. Sun, Y. Z. Tan, S. B. Yang, X. L. Feng and K. Mullen, *J. Am. Chem. Soc.*, 2012, **134**, 19532–19535.
21 A. P. Singh, M. Mishra, P. Sambyal, B. K. Gupta, B. P. Singh, A. Chandra and S. K. Dhawan, *J. Mater. Chem. A*, 2014, **2**, 3581–3593.
22 J. J. Liang, Y. F. Xu, D. Sui, L. Zhang, Y. Huang, Y. F. Ma, F. F. Li and Y. S. Chen, *J. Phys. Chem. C*, 2010, **114**, 17465–17471.
23 X. Sun, J. P. He, G. X. Li, J. Tang, T. Wang, Y. X. Guo and H. R. Xue, *J. Mater. Chem. C*, 2013, **1**, 765–777.
24 A. G. D. Aloia, F. Marra, A. Tamburrano, G. D. Bellis and M. S. Sarto, *Carbon*, 2014, **73**, 175–184.
25 M. J. Hu, J. F. Gao, Y. C. Dong, K. Li, G. C. Shan, S. L. Yang and R. K. Y. Li, *Langmuir*, 2012, **28**, 7101–7106.
26 W. L. Song, L. Z. Fan, M. S. Cao, M. M. Lu, C. Y. Wang, J. Wang, T. T. Chen, Y. Li, Z. L. Zhou, J. Liu and Y.-P. Sun, *J. Mater. Chem. C*, 2014, **2**, 5057–5064.
27 W. L. Song, J. Wang, L. Z. Fan, Y. Li, C. Y. Wang and M. S. Cao, *ACS Appl. Mater. Interfaces*, 2014, **6**, 10516–10523.
28 J. G. Park, J. Louis, Q. F. Cheng, J. W. Bao, J. Smithyman, R. Liang, B. Wang, C. Zhang, J. S. Brooks, L. Kramer, P. Fanchasis and D. Dorough, *Nanotechnology*, 2009, **20**, 415702.
29 X. Huang, X. Y. Qi, F. Boey and H. Zhang, *Chem. Soc. Rev.*, 2012, **41**, 666–686.
30 K. Yang, L. Z. Feng, X. Z. Shi and Z. Liu, *Chem. Soc. Rev.*, 2013, **42**, 530–547.
31 Y. P. Zhai, Y. Q. Dou, D. Y. Zhao, P. F. Fulvio, R. T. Mayes and S. Dai, *Adv. Mater.*, 2011, **23**, 4828–4850.
32 S. Park and R. S. Ruoff, *Nat. Nanotechnol.*, 2009, **4**, 217–224.
33 D. R. Dreyer, S. Park, C. W. Bielawski and R. S. Ruoff, *Chem. Soc. Rev.*, 2010, **39**, 228–240.
34 C. K. Chua and M. Pumera, *Chem. Soc. Rev.*, 2014, **43**, 291–312.
35 Z. Weng, Y. Su, D. W. Wang, F. Li, J. H. Du and H. M. Cheng, *Adv. Energy Mater.*, 2011, **1**, 917–922.
36 L. L. Peng, X. Peng, B. R. Liu, C. Z. Wu, Y. Xie and G. H. Yu, *Nano Lett.*, 2013, **13**, 2151–2157.
37 G. K. Wang, X. Sun, F. Y. Lu, H. T. Sun, M. P. Yu, W. L. Jiang, C. S. Liu and J. Lian, *Small*, 2012, **8**, 452–459.
38 D. S. Yu, K. L. Goh, H. Wang, L. Wei, W. C. Jiang, Q. Zhang, L. M. Dai and Y. Chen, *Nat. Nanotechnol.*, 2014, **9**, 555–562.
39 Y. L. Ren, H. Y. Wu, M. M. Lu, Y. J. Chen, C. L. Zhu, P. Gao, M. S. Cao, C. Y. Li and Q. Y. Ouyang, *ACS Appl. Mater. Interfaces*, 2012, **4**, 6436–6442.
40 K. W. Putz, O. C. Compton, C. Segar, Z. An, S. T. Nguyen and L. C. Brinson, *ACS Nano*, 2011, **5**, 6601–6609.
41 G. E. Brown, V. E. Henrich, W. H. Casey, D. L. Clark, C. Eggleston, A. Felmy, D. W. Goodman, M. Gratzel, G. Maciel, M. I. McCarthy, K. H. Nealson, D. A. Sverjensky, M. F. Toney and J. M. Zachara, *Chem. Rev.*, 1999, **99**, 77–174.
42 D. Micheli, R. Pastore, C. Apollo, M. Marchetti, G. Gradoni, V. M. Primiani and F. Moglie, *IEEE Trans. Microwave Theory Tech.*, 2011, **59**, 2633–2646.
43 D. Michell, C. Apollo, R. Pastore and M. Marchetti, *Compos. Sci. Technol.*, 2010, **70**, 400–409.
44 M. Mahmoodi, M. Arjmand, U. Sundararaj and S. Park, *Carbon*, 2012, **50**, 1455–1464.

45 D. Micheli, *Radar absorbing materials and microwave shielding structure design*, LAP Lambert Academic Publishing AG & Co. KG, 2012, pp. 21–122.
46 D. R. Smith and N. Kroll, *Phys. Rev. Lett.*, 2000, **85**, 2933–2936.
47 B. Bleaney and B. I. Bleaney, *Electricity and Magnetism*, Cambrige University Press, 3rd edn, 1976.
48 M. S. Cao, W. L. Song, Z. L. Hou, B. Wen and J. Yuan, *Carbon*, 2010, **48**, 788–796.
49 Z. J. Wang, L. N. Wu, J. G. Zhou, W. Cai, B. Z. Shen and Z. H. Jiang, *J. Phys. Chem. C*, 2013, **117**, 5446–5452.
50 J. P. Zou, Z. Z. Wang, M. Q. Yan and H. Bi, *J. Phys. D: Appl. Phys.*, 2013, **47**, 275001.
51 P. B. Liu and Y. Huang, *RSC Adv.*, 2013, **3**, 19033–19039.
52 H. B. Zhang, Q. Yan, W. G. Zheng, Z. X. He and Z. Z. Yu, *ACS Appl. Mater. Interfaces*, 2011, **3**, 918–924.
53 J. Q. Ling, W. T. Zhai, W. W. Feng, B. Shen, J. F. Zhang and W. G. Zheng, *ACS Appl. Mater. Interfaces*, 2013, **5**, 2677–2684.
54 S. Maiti, N. K. Shrivastava, S. Suin and B. B. Khatua, *ACS Appl. Mater. Interfaces*, 2013, **5**, 4712–4724.
55 W. L. Song, M. S. Cao, M. M. Lu, J. Yang, H. F. Ju, Z. L. Hou and L. Z. Fan, *Nanotechnology*, 2013, **24**, 115708.
56 Y. W. Cheng, S. T. Lu, H. B. Zhang, C. V. Varanasi and J. Liu, *Nano Lett.*, 2012, **12**, 4206–4211.
57 W. Hummers and R. O. Fleman, *J. Am. Chem. Soc.*, 1958, **80**, 1339.